

AKARI infrared imaging of reflection nebulae IC4954 and IC4955

Daisuke ISHIHARA^{1,*}, Takashi ONAKA¹, Hidehiro KANEDA², Toyoaki SUZUKI²,
Hirokazu KATAZA², Itsuki SAKON¹, Yoko OKADA²,
Yasuo DOI³, Naofumi FUJISHIRO², Hideaki FUJIWARA¹, Yoshifusa ITA², Tuneo KII²,
Woojung KIM², Sin'itirou MAKIUTI², Toshio MATSUMOTO², Hideo MATSUHARA²,
Hiroshi MURAKAMI², Takao NAKAGAWA², Youichi OHYAMA², Shinki OYABU²,
Stephen SERJEANT⁴, Hiroshi SHIBAI⁵, Toshinobu TAKAGI², Toshihiko TANABÉ⁶,
Kazunori UEMIZU¹, Munetaka UENO³, Fumihiko USUI², Takehiko WADA²,
and

Hidenori WATARAI⁷

**e-mail: ishihara@astron.s.u-tokyo.ac.jp*

¹*Department of Astronomy, Graduate School of Science, The University of Tokyo,
Bunkyo-ku, Tokyo 113-0033, Japan*

²*Institute of Space and Astronautical Science, Japan Aerospace Exploration Agency,
3-1-1 Yoshinodai, Sagamihara, Kanagawa 229-8510, Japan*

³*Department of Earth Science and Astronomy, University of Tokyo, 3-8-1 Komaba,
Meguro-ku, Tokyo 153-8902, Japan*

⁴*Astrophysics Group, Department of Physics and Astronomy,
The Open University, Milton Keynes MK7 6AA*

⁵*Graduate School of Science, Nagoya University,
Furu-cho, Chikusa-ku, Nagoya 464-8602, Japan*

⁶*Institute of Astronomy, University of Tokyo, 2-21-1 Osawa, Mitaka, Tokyo 181-0015, Japan*

⁷*Office of Space Applications, Japan Aerospace Exploration Agency,
Tsukuba, Ibaraki, 305-8505, Japan*

(Received 2007 March 22; accepted)

Abstract

We present the observations of the reflection nebulae IC4954 and IC4955 region with the Infrared Camera (IRC) and the Far-Infrared Surveyor (FIS) on board the infrared astronomical satellite AKARI during its performance verification phase. We obtained 7 band images from 7 to 160 μm with higher spatial resolution and higher sensitivities than previous observations. Among the 7 band images, the S11 (11 μm) data provide the highest spatial-resolution and most sensitive image, in which 10 point-like sources are newly detected in the mid-infrared and IC4955 is resolved into

two condensations. The mid-infrared images show distinct arc-like structures, inside of which bright sources in the L18W image are located. The mid-infrared color of the S9W ($9\mu\text{m}$) and L18W ($18\mu\text{m}$) bands shows a systematic variation around the exciting sources. It is red in the vicinity of the exciting sources, whereas it becomes blue in the surrounding regions. This can be interpreted in terms of the decreasing contribution of thermal emission from dust grains in equilibrium with the incident radiation field as the distance from the exciting source increases. The spatial variation in the mid-infrared color suggests that the star-formation in IC4954/4955 is progressing from south-west to north-east. The FIS data also clearly resolve two nebulae for the first time in the far-infrared. The FIS 4-band data from $65\mu\text{m}$ to $160\mu\text{m}$ allow us to correctly estimate the total infrared luminosity from the region, which is about one sixth of the energy emitted from the existing stellar sources. There is little possibility for the presence of embedded massive stars that have escaped detection. Five candidates for young stellar objects have been detected as point sources for the first time in the $11\mu\text{m}$ image. They are located in the red S9W to L18W color regions, suggesting that current star-formation has been triggered by previous star-formation activities. A wide area map of the size of about $1^\circ \times 1^\circ$ around the IC4954/4955 region was created from the AKARI mid-infrared all-sky survey data. Together with the HI 21 cm data, it suggests a large hollow structure of a degree scale, on whose edge the IC4954/4955 region has been created, indicating star formation over three generations in largely different spatial scales.

Key words: infrared: ISM — open cluster: individual (Roslund 4) — nebulae: individual (IC4954 and IC4955) — stars: star formation

1. Introduction

The reflection nebulae IC4954 and IC4955 are located in the Vulpecula constellation on the Galactic plane around $(l, b) = (66.96^\circ, -1.26^\circ)$. These nebulae are associated with the young open cluster Roslund 4 (Roslund 1960). The heliocentric distance and the age of this cluster are estimated based on the analysis of isochrones as 10 Myr and 2.9 kpc by Racine (1996), 4 Myr and 2 kpc by Phelps (2003) (hereafter P03), and 15 Myr and 2 kpc by Delgado et al. (2004) (hereafter D04). These studies suggest the presence of stars of a relatively wide age range and on-going star-formation in the IC4954/4955 region. In this paper we assume the distance to be 2 kpc. P03 and D04 also detected three active regions in [SII] images and some of them are classified as Herbig Haro objects. The $\text{H}\alpha$, [NII] and [SII] emission lines from the cluster members are detected in optical spectroscopic observations (D04). This region is an interesting place for the study of star-formation process because of the co-existence of both

young and relatively old populations (P03; D04). Except for the dedicated observation of D04, the parallax, radial velocity, proper motions and spectral type of the cluster members (or clues for the identification of the members) are largely unavailable in existing catalogs because of its far heliocentric distance.

^{12}CO observations show that at least one cloud of $10^5 M_{\odot}$ is associated with this region (Leisawitz et al. 1989). In the infrared, these nebulae are observed in the IRAS and MSX Galactic surveys. The IRAS Point Source Catalog (PSC) has entries of three point sources in this region, whereas the MSX map shows distinguished structures in four mid-infrared bands of A($8.28 \mu\text{m}$), C($11.2 \mu\text{m}$), D($14.3 \mu\text{m}$) and E($21.34 \mu\text{m}$). However, the poor spatial resolution of IRAS and the insufficient sensitivity of the MSX $21 \mu\text{m}$ prevent us from making detailed analysis of this interesting region in the infrared. This region is not included in the Galactic Legacy Infrared Mid-Plane Survey Extraordinaire with *Spitzer* (GLIMPSE; Benjamin et al. 2003).

AKARI is the first Japanese infrared astronomical satellite dedicated for infrared astronomy (Murakami et al. 2007). It has two scientific instruments: the Infrared Camera (IRC; Onaka et al. 2007b) that covers near- and mid-infrared wavelengths of $2\text{--}26 \mu\text{m}$, and the Far-Infrared Surveyor (FIS; Kawada et al. 2007) that covers the far-infrared spectral range of $50\text{--}200 \mu\text{m}$. The performance of both instruments has been confirmed by observations during the performance verification (PV) phase from 2006 April 24 to May 8. The present paper reports the results of observations of the IC4954/4955 region with both IRC and FIS taken mainly during the PV phase.

The observations and data reduction are described in §2. The observational results are shown in §3. The nature and the origin of the Roslund 4 region are discussed in § 4. Finally, we summarize the results in §5.

2. Observations and Data reductions

AKARI seven band images were taken by two scientific instruments with three kinds of operation mode. The observational parameters are summarized in Table 1.

2.1. IRC All-Sky Survey (9 and $18 \mu\text{m}$)

The S9W ($9 \mu\text{m}$) and L18W ($18 \mu\text{m}$) data of the IC4954/4955 region were taken as part of the all-sky survey observations. Both data were taken simultaneously with different channels of the IRC, MIR-S and MIR-L, which observe sky positions separated by about $20'$ in the cross-scan direction (Onaka et al. 2007b). In the all-sky survey, the IRC is operated in the scan mode (Ishihara et al. 2006a), in which the data of only two rows in the detector arrays are taken with the cross-scan width of about $10'$. The scan speed is about $215'' \text{s}^{-1}$. The output signals of every four adjacent pixels are binned together to reduce the data down-link rate and the virtual pixel scale is $9.''36 \times 9.''36$ in the survey mode. The seconds confirmation is enabled by the

Table 1. Observational parameters for IC4954/4955 by AKARI

λ_{ref} (μm)	$\Delta\lambda$ (μm)	FWHM ($''$)	Pix scale ($''\times''$)	Scan speed ($''\text{ s}^{-1}$)	Instrument	Filter	AOT
9	4.10	5.5	9.36 \times 9.26	215	IRC	S9W	ASS
11	4.12	4.8	1.23 \times 2.34	30	IRC	S11	IRC51
18	9.97	5.7	9.36 \times 9.36	215	IRC	L18W	ASS
65	21.7	37	26.8 \times 26.8	15	FIS	N60	FIS01
90	37.9	39	26.8 \times 26.8	15	FIS	WIDE-S	FIS01
140	52.4	58	44.2 \times 44.2	15	FIS	WIDE-L	FIS01
160	34.1	61	44.2 \times 44.2	15	FIS	N160	FIS01

independent data sets taken by the two separated rows, which allow to efficiently reject high-energy ionization particle events and largely improves the reliability of the source detection. Finer spatial information as well as improved sensitivity can be expected in the data reduction process because two rows are sampled and binned in an interlaced manner and the observed strip is shifted by $4'$ in adjacent scan paths with a given region being observed more than twice on average. The reset interval is set as 13.5 s, which corresponds to 306 samplings or 48.9' in the scanning direction. The length of a reset in the all-sky survey is set as 2.2 ms (hereafter long reset). The IC4954/4955 region was observed during 2006 May 1–8 in the PV phase with the descending path of $d\beta/dt < 0$ and 2006 November 1–8 with the ascending path of $d\beta/dt > 0$, where β is the ecliptic latitude. Both data are averaged with median in the present analysis. The difference between the two data sets is less than 10% in the sky brightness.

Fragments of the data sets covering IC4954/4955 are retrieved from the IRC all-sky survey database and reduced automatically by the pipeline software to create a map (Ishihara et al. 2007). The pipeline process includes linearity correction, flat correction, reset anomaly correction (see below), source extraction, rejection of high-energy particle events by the seconds confirmation, position determination using identified objects, coaddition of the images obtained by the two rows, and map construction.

The flux calibration of point sources in the all-sky survey data are carried out based on a large number of detections of hundreds of stars in the standard star networks (Cohen et al. 1999; Cohen et al. 2003; Ishihara et al. 2006b). The flux accuracy is estimated as $\sim 7\%$ for the S9W band and $\sim 15\%$ for the L18W band for point sources at the present calibration stage. The detection limits (5σ) for point sources are estimated as 50 mJy for the S9W band and 120 mJy for the L18W band. The calibration for diffuse emission is on-going and a relative error of 30% is assigned at present.

Positions of the detected objects were first estimated based on the data of the gyroscopes and the star trackers on board and then refined by using the positions of bright ($K < 8$ mag) 2MASS PSC sources. The position accuracy is estimated to be $5''$ at present.

2.2. IRC Slow Scan ($11\mu\text{m}$)

The S11 ($11\mu\text{m}$) band image was obtained during the PV phase with the IRC slow scan mode of the Astronomical Observation Template (AOT) IRC51. IRC51 is a set of round-trip scans designed for mapping of a small area of up to $\sim 10' \times 120'$ in about 15 min of a pointed observation (Murakami et al. 2007; Onaka et al. 2007b). A higher sensitivity than in the all-sky survey and a wider sky coverage than in imaging observations can be achieved in this observation mode. It also allows to observe very bright sources, such as IC4954/4955, which will be saturated in the imaging observation. The scan speed was set as $30''\text{s}^{-1}$ and the S11 filter was selected. The observation of IC4954/4955 was carried out on 2006 May 1.

The focal plane arrays were operated in the same scan mode as in the all-sky survey observations except that the data binning is not made and the full spatial information is obtained in the cross-scan direction. Confirmation of source detection was made by round-trip scans. The grid size of slow scan observations is set as $1.''32 \times 2.''34$. It is determined by the physical pixel size in the cross-scan direction ($2.''34$), and by the sampling rate and the scan speed in the scanning direction ($1.''32$). It oversamples the image size of the imaging mode at $11\mu\text{m}$ ($\sim 4.''8$; Onaka et al. 2007b). The time spent for a reset was shortened to $68\mu\text{s}$ (short reset). The charge integration curve shows an anomalous behavior immediately after a reset (reset anomaly). The magnitude of this effect depends on the time spent for a reset. We confirm that the short reset significantly improves the reset anomaly effect. Gaps in the observed area due to the reset was thus reduced thanks to the combination of the slower scan speed and the short reset. The reset period was also shortened to 2.24s because the gap due to the reset could be ignored. Consequently the effect of saturation was also reduced. There is a drift in the offset level owing to the temperature drift (Ishihara et al. 2003). It is corrected by referring to the signal level during the reset. The signal during the reset corresponds to the output with the input blocked, and thus indicates the offset level of the preamplifier. The detection limit is determined by the read-out noise of the detector rather than the zodiacal background fluctuation because of the short sampling time.

The data reduction largely follows that for the all-sky survey except for a few parameters adjusted for the finer pixels, such as flat correction, and a custom-designed map reconstruction module is developed. At first the data taken in a single scan are arranged into a $10' \times 60'$ strip image by assuming that the sampling rate and the scan speed of the satellite are constant. Individual sets of images obtained by two separated rows are aligned with each other and coadded into a combined image. The position reconstruction of the map is made based on the association with detected 2MASS sources as in the all-sky survey data. The positional accuracy of the data is estimated to be $5''$ at present.

The in-flight calibration of the IRC has been carried out for all the imaging filters in pointed imaging observations based on observations of the standard star networks (Onaka et al. 2007b). For the all-sky observations and slow-scan observations, however, most observa-

tions have been made only with the S9W and L18W bands. The flux calibration for the S11 ($11\ \mu\text{m}$) band image in the slow-scan observations is performed in an indirect way because no observations of standard stars have been made in the same scan speed with the same filter. First, the calibration for the S9W in the slow-scan mode with the scan speed of $30''\ \text{s}^{-1}$ is made by the comparison of fluxes derived from slow-scan observations with those from the all-sky survey for the same stars. Then the calibration for the S11 band with the scan speed of $30''\ \text{s}^{-1}$ is estimated by assuming the relative calibration between the S9W and S11 bands in pointed imaging observations. Taking account of the uncertainties in the indirect calibration, we set a conservative uncertainty of 30% in the S11 data at present.

2.3. FIS Slow Scan ($65, 90, 140, 160\ \mu\text{m}$ band)

FIS observations of IC4954/4955 were executed with N60 ($65\ \mu\text{m}$), WIDE-S ($90\ \mu\text{m}$), WIDE-L ($140\ \mu\text{m}$), and N160 ($160\ \mu\text{m}$) bands in the 2-round-trip slow-scan mode (FIS01) with a scan speed of $15''\text{s}^{-1}$ on 2006 May 3. The four-band data were taken simultaneously with correlated double sampling (CDS) in about 15 min of a pointed observation. Details of the observation scheme and the data reduction of the FIS slow scan data are described in Kaneda et al. (2007b) and Suzuki et al. (2007). At present, the systematic flux calibration errors for the CDS mode are estimated to be 30, 40, 50, and 50% for N60, WIDE-S ($90\ \mu\text{m}$), WIDE-L ($140\ \mu\text{m}$), and N160, respectively. The relative position accuracy among the FIS bands is better than $10''$ because they were taken simultaneously, but the absolute accuracy is estimated to be about $1'$. Thus all the FIS images are aligned relative to the IRC images in the equatorial coordinates. Since the IRC data were taken at a different epoch from that of FIS, the relative position accuracy is estimated to be about $30''$ at present.

3. Results

3.1. Infrared images of IC4954 and IC4955

The images of IC4954/4955 in AKARI S9W, S11, L18W, N60, WIDE-S ($90\ \mu\text{m}$), WIDE-L ($140\ \mu\text{m}$), and N160 bands are shown in figure 1. The northern nebula in the image is IC4955 (enclosed by the green line in figure 1a) and the southern nebula is IC4954 (enclosed by the red line). The AKARI images reveal several distinct characteristics of the nebulae.

The AKARI S9W map by the all-sky survey is created with a grid size of $1.''56 \times 1.''56$ from the virtual pixel size of $9.''36 \times 9.''36$. It is in good agreement with the MSX A-band ($8.28\ \mu\text{m}$) image. The AKARI S9W band has a better spatial resolution and the relative spectral response similar to that of MSX A-band except for the inclusion of the $11.2\ \mu\text{m}$ unidentified infrared (UIR) band (Onaka et al. 2007b). Three IRAS point sources exist in this region as indicated in the S9W image. The location of IRAS 20026+2906 does not match with the bright spot in the S9W images (source F in figure 1b) probably due to the complicated background structures in this region.

The S11 image has the finest resolution and the deepest sensitivity among the seven bands owing to its observing mode. Point-like objects are clearly resolved and denoted by A–L (for details see §3.2). Distinct extended structures are denoted by $a-h$. The northern nebula IC4955 is spatially resolved into two condensations (a and d) and two arc-like structures (b and c). The two arcs may overlap with each other on the line-of-sight. Arc-like structures are also found in IC4954 (e and f). All the arcs point toward the north-east of the nebulae and extend over the outer edge of the nebula emission in the optical image.

The AKARI L18W image has a higher signal-to-noise ratio and higher spatial resolution than the MSX E-band ($21.2\,\mu\text{m}$) image. Point-like objects ($g-n$) are clearly seen in figure 1c. The spatial distribution of the $18\,\mu\text{m}$ emission seems to be significantly different to that of the S9W or S11 emission. See §4.1 for the discussion on the morphologies of the S9W and L18W images.

The AKARI N60 ($65\,\mu\text{m}$) and WIDE-S ($90\,\mu\text{m}$) image surpass the *IRAS* 60 or $100\,\mu\text{m}$ images. The two nebulae are spatially resolved in this wavelength range for the first time. The faint arc-like structure toward the south-east is also detected. The WIDE-L ($140\,\mu\text{m}$) and N160 ($160\,\mu\text{m}$) data are unique to AKARI. These two bands make significant constraints on the dust emission (figure 2) for the estimate of the total infrared luminosity (§ 4.1).

The total fluxes from IC4954 and IC4955 are derived from the integrated signals in the regions enclosed by the red and green lines in figure 1a and the sky background is estimated from the surrounding region and subtracted. The results of IC4954 and IC4955 are summarized in Table 2 and their spectral energy distributions (SEDs) are plotted in figure 2. The uncertainties in Table 2 include the systematic errors. The MSX image data at band A ($8.28\,\mu\text{m}$), C ($12.13\,\mu\text{m}$), D ($14.65\,\mu\text{m}$), and E ($21.3\,\mu\text{m}$) are also integrated over the same regions and the sky background is subtracted similarly. The results are plotted in figure 2. Except for the band D data, the IRC data are in fair agreement with the MSX data, taking account of the uncertainties and the differences in the band profiles. The band D data are fainter even compared to other MSX band data for both nebulae.

In figure 2 also plotted are the *IRAS* PSC data. It is not possible to estimate the fluxes for IC4954 and IC4955 directly from the *IRAS* data since the sources are not clearly resolved. In the figure, the fluxes of *IRAS* 20028+2903 are plotted as IC4954, whereas the sum of the fluxes of *IRAS*0026+2906 and *IRAS*2007+2905 are indicated as IC4955. Except for the $60\,\mu\text{m}$ data, the *IRAS* fluxes are lower than the AKARI/IRC and FIS fluxes and the agreement is not very good. The difference can be attributed to the fact that the *IRAS* data do not include the diffuse emission correctly in addition to the position mismatch of *IRAS* 20026+2906.

3.2. Newly detected point-like sources

The fluxes and positions of 12 point-like objects detected in the S11 image (indicated by A–L in figure 1b) are summarized in Table 3. They all have corresponding 2MASS sources as

Table 2. Photometric results of IC4954 and IC4955*

AKARI/IRC results							
Object	S9W	S11	L18W	N60	WIDE-S	WIDE-L	N160
	9 μm	11 μm	18 μm	65 μm	90 μm	140 μm	160 μm
IC4954	62.2 \pm 18.7	61.1 \pm 18.3	56.2 \pm 16.9	790 \pm 240	860 \pm 260	2500 \pm 1000	1890 \pm 570
IC4955	33.6 \pm 10.1	33.4 \pm 10.2	31.2 \pm 9.36	330 \pm 100	340 \pm 100	1700 \pm 680	850 \pm 260
MSX data							
name	8.28 μm	12.13 μm	14.65 μm	21.34 μm			
IC4954	55.15 \pm 0.26	75.15 \pm 2.25	32.29 \pm 1.29	66.84 \pm 4.01			
IC4955	28.86 \pm 1.44	40.25 \pm 1.21	16.10 \pm 0.64	36.21 \pm 2.17			
IRAS PSC sources							
IRAS name	12 μm	25 μm	60 μm	100 μm			
20026+2906	2.741 \pm 0.66	<0.25	<3.186	<66.76			
20027+2905	3.356 \pm 0.30	14.06 \pm 0.70	<540.3	<50.71			
20028+2903	20.26 \pm 0.81	47.29 \pm 1.89	540.3 \pm 48.6	1177 \pm 129			

* Units are in Jy.

indicated in the table. The SED of each source is plotted in figure 3, including the 2MASS data. There is a MSX source (G066.9971-01.2247) close to source F, whose C band flux (12.13 μm) is much larger than the S11 flux (see Table 3), suggesting that the MSX flux includes contributions from the surrounding diffuse emission since the source is located in an extended emission region. In the vicinity of source K, there are two MSX sources (G066.9646-01.2783 and G066.9609-01.2776), whose C band fluxes are also very large (see Table 3). G066.9646-01.2783 seems to correspond to source K in position and G066.9609-01.2776 seems to be located close to another optically bright source, 2MASS 20045331+2911469, around which the S11 image does not detect any point source. The large MSX fluxes can also be attributed to the diffuse emission around the source. Except for F and K, 10 sources are detected as point sources for the first time in the mid-infrared by the present IRC observations.

4. Discussion

4.1. Infrared characteristics of IC4954 and IC4955

The total infrared luminosity from the nebular region can be estimated from the AKARI observations. The AKARI IRC and FIS data (figure 2) are fitted by a three-temperature dust model with the emissivity proportional to λ^{-2} . The three temperatures are fixed as 20, 40, and 230 K for both nebulae. The fitted models are shown by the solid and dotted lines in figure 2 for IC4954 and IC4955, respectively. The total infrared luminosity L_{IR} is then calculated by

Table 3. Point sources detected in the S11 image

ID	R.A.	Decl.	2MASS ID	11 μ m flux	MSX source	MSX band C flux
	(J2000.0)			(mJy)		(Jy)
A	20 04 56	+29 11 17	20045681+2911154	6.7 \pm 0.3		
B	20 04 46	+29 11 16	20044653+2911167	19.6 \pm 0.3		
C	20 04 49	+29 11 48	20044974+2911486	55.6 \pm 1.2		
D	20 04 43	+29 12 49	20044366+2912496	13.1 \pm 0.3		
E	20 04 45	+29 13 39	20044585+2913389	22.3 \pm 0.5		
F	20 04 45	+29 15 14	20044568+2915152	23.0 \pm 0.8	G066.9971-01.2247	3.4441
G	20 04 44	+29 13 50	20044473+2913512	7.7 \pm 0.2		
H	20 04 46	+29 10 21	20044676+2910221	5.2 \pm 0.2		
I	20 04 47	+29 09 59	20044710+2910006	39.2 \pm 0.4		
J	20 04 50	+29 11 05	20045044+2911060	45.7 \pm 1.1		
K	20 04 52	+29 11 43	20045278+2911435	208.5 \pm 4.4	G066.9646-01.2783*	5.4393
					G066.9609-01.2776 [†]	3.6187
L	20 04 54	+29 12 07	20045478+2912080	14.3 \pm 0.3		

* Most probable MSX source that corresponds to K.

[†] No corresponding point source in the S11 image (see text).

$$L_{\text{IR}} = \sum_{i=1}^3 \int C_i B(T_i, \lambda) \lambda^{-2} d\lambda,$$

where $T_i = 20, 40$, and 230 K for $i = 1, 2$, and 3 , respectively, and C_i is the fitting constants. We obtain $L_{\text{IR}} = 9.5 \times 10^3$ and $4.2 \times 10^3 L_{\odot}$ for IC4954 and IC4955, respectively, the sum of the two nebulae being $1.4 \times 10^4 L_{\odot}$.

The stellar luminosity available for dust heating can be estimated by summing up the stellar luminosity L_* of all the stars located in the region as

$$L_{\text{stellar}} = \sum_{\text{members}} L_*.$$

The luminosity of each star is estimated simply based on its spectral type with the assumption that they are on the main sequence (Schmidt-Kaler 1982; Johnson 1996; De Jager et al. 1987). We select 13 stars that have known spectral types and are assigned to the member of this region (D04). We also select other 11 stars whose spectral types are estimated to be earlier than B7 based on their color. A total of 24 stars in this region are included in the estimate of L_{stellar} . The spectral type is taken from the spectroscopic classification or estimated from the reddening corrected $U - B$ and $B - V$ in D04. The membership assignment and the UBVRI photometric results (D04) were obtained from WEBDA¹. The location of the 24 stars used in the estimation is shown by the crosses in figure 4a. The O8en star reported in Merrill

¹ <http://obswww.unige.ch/webda>

et al. (1942) located in the south-west of the nebulae (shown in figure 4b) is not included in the estimation because it seems to be too far from the nebula region. Even if we include this star, the total stellar luminosity will be increased only by 15%, and it will not affect the present conclusion. The total stellar luminosity in this region thus estimated is $8.3 \times 10^4 L_{\odot}$. It is about 6 times of L_{IR} . Leisawitz & Hauser (1988) have indicated that typically only a small fraction (~ 0.2) of the cluster luminosity is absorbed by dust grains. The present result is in good agreement with their results, suggesting that it is not very likely that there are very luminous stars hidden in dusty environments in this region.

With the dust mass emissivity at $100 \mu\text{m}$ being 0.6 g cm^{-2} (Hildebrand 1983), the dust mass associated with IC4954 and IC4955 is derived to be about 40 and 20 M_{\odot} , respectively. The typical size of the nebulae is estimated from the intensity contours of 10% of the peak to be about 1.3 or $2 \times 10^{18} \text{ cm}$. Assuming that the gas-to-dust ratio is 100, the average gas density of the infrared emitting medium is estimated to be about $(2 - 4) \times 10^5 \text{ cm}^{-3}$. This is in the range of the density of dense photo-dissociation regions (PDRs), such as the Orion region (Tielens & Hollenbach 1985), indicating that the IC4954/4955 region is still a young star-forming region rather than diffuse PDRs, such as the Carina nebula (Mizutani et al. 2004).

The color images of IC4954/4955 in the optical, mid-infrared, and far-infrared are shown in figure 4. In the mid-infrared, the spatial distribution of the $9 \mu\text{m}$ emission is similar to that of the $11 \mu\text{m}$ emission, whereas the difference in the spatial distribution between S9W and L18W images is remarkable. Figure 5 shows the relative spectral response of the S9W, S11, and L18W bands. Also plotted by the thin solid line is an interstellar cirrus spectrum taken with *Spitzer*/IRS for a reference. The S9W band includes the major UIR bands at 6.2 , 7.7 , 8.6 , and $11.2 \mu\text{m}$ except for the $12.7 \mu\text{m}$ band, and is not affected by the continuum emission longer than $12 \mu\text{m}$. The S11 band is affected by only part of the UIR $7.7 \mu\text{m}$, but includes the UIR 11.2 and $12.7 \mu\text{m}$, and the $[\text{NeII}]12.8 \mu\text{m}$ line emission. In the L18W the UIR $17 \mu\text{m}$ complex is included and the main contributor is the continuum emission longer than $15 \mu\text{m}$. No appreciable difference seen between the S9W and S11 images suggests that the spectrum shape between 6 to $13 \mu\text{m}$ does not vary significantly in the region and that the line emissions from ionized species is insignificant compared to the UIR band emission. The difference between S9W and L18W should be related to the variation in the continuum emission longer than $15 \mu\text{m}$. The S9W image shows arc-like structures clearly and the L18W image indicates high concentration of the emission in narrow areas. The difference can be seen noticeably in the mid-infrared color image (figure 4b). The emission in L18W is stronger inside the arcs as indicated by red. Most of the regions highlighted by red color are associated with B-type stars, which are supposed to play as heating sources of the region: in the region *g*, there are a B and a B9 star; the region *h* is associated with a B2 and a B7 star; a B-type star in the region *n* is suggested to not belong to the member of this region on the basis of the radial velocity (D04) and thus may not be related to this region. The other nearby B5 star must be a heating source of this

region. The red regions match also with bright regions in the $H\alpha$ image (D04). We surmise that the red regions are directly heated by B-type stars and probably associated with ionized gas, whereas the arcs represented by white color in figure 4b are PDRs surrounding them, which are characterized by the strong UIR emissions in the S9W (cf., Onaka 2004). The strength of the incident radiation field at the arcs (b , c , and f) is estimated based on the projected distance from these heating sources as 900, 3000, and 800, respectively, in units of the solar neighborhood value ($1.6 \times 10^{-6} \text{ W m}^{-2}$, Habing 1968). These are comparable with those of typical PDRs (cf., Mizutani et al. 2004).

IRAS observations indicate the increase of the ratio of $25 \mu\text{m}$ to $12 \mu\text{m}$ intensities in the vicinity of heating sources for several cases (Boulanger et al. 1988; Ryter et al. 1987). The UIR band emission largely contributes to the IRAS $12 \mu\text{m}$ band. The variation in the intensity ratio has been attributed to the increasing contribution from thermal emission of large grains rather than the destruction of the UIR band carriers. Recent investigations on the infrared diffuse radiation of our Galaxy and the Large Magellanic Cloud have in fact shown that the variations in the infrared SED of the diffuse emission can reasonably be interpreted in terms of a superposition of the model emissions, in which the contribution from dust grains in radiative equilibrium becomes large in the vicinity of heating sources together with the effect of destruction of the UIR band carriers in strong radiation fields (Sakon et al. 2006; Onaka et al. 2007a). The band profile of the IRC S9W is shifted to shorter wavelengths compared to the IRAS $12 \mu\text{m}$ band and thus S9W probes the UIR band emission more sensitively and is less subject to thermal emission in longer wavelengths (Onaka et al. 2007b). Consequently the effect of thermal emission near the exciting source appears clearly in the color map of S9W/S11/L18W. The red color in figure 4 points to the region strongly heated by heating sources, whereas the white color indicates the region where the UIR band emission is dominant. The observed color variation is well accounted for by the increasing contribution from thermal dust emission. It further indicates that the UIR-band dominating infrared bright regions (white in figure 4b) are always located in the north-east side, suggesting the presence of high density regions in this side.

To examine the distribution of young stellar object (YSO) candidates in this region, objects with red color in the near-infrared are selected from the 2MASS catalog. The interstellar reddening to the IC4954/4955 region is estimated to be $E(B - V) = 0.91$ (D04), which corresponds to $(H - K) = 0.18$ (Rieke & Lebofsky 1985). Taking account of the internal extinction, we conservatively set the criteria that $H - K > 0.9$ and $J - H > 0.9$ to select YSO candidates. They are shown by the red circles and other blue 2MASS sources are indicated by the blue circles in figure 4b. Most of them are located in the white color region as well as in between the two nebulae, where the optical image shows few stars (see below). Only a few red objects are present inside the arcs, indicating that YSO candidates are concentrated in dense regions slightly away from those directly heated by B-type stars. Five of the 2MASS red objects are

detected in the S11 image (C, F, J, K, and L). All of them show YSO-like SEDs in the near-to mid-infrared (§ 3.2; cf., Whitney et al. 2003; Reach et al. 2004), supporting the validity of the adopted criteria. There is also one red object in the relatively red color region without any corresponding early-type stars. It may also play a role of an embedded heating source in the region. A summary of the relations among the various extended (a – n) point-like sources is given in Table 4.

Table 4. Structures and point sources in the mid-infrared of the IC4954/4955 region

S11		S18W	Comments
Extended	Point-like	Extended	
a	F	g	The peak positions of a and g do not coincide. F is located at the peak of a .
b		i	The peak positions do not coincide. There may be a hidden source at i .
c	E, G	h	The peak positions of c and h do not coincide. E and G are heating sources for h .
d		j	The peak positions are matched within the uncertainties.
	K	k, l	K coincides with k . No counterpart is seen for l .
	A	n	The position of A coincides with n . A is listed as a non-member.
	J	m	J is a heating source for m .

Comparison of figures 4a and c indicates that the density of stars is low in between IC4954 and IC4955 in the optical image, whereas the dust emission is seen in the corresponding region in the WIDE-L ($140\ \mu\text{m}$) image. The size of the region ($120''$) is sufficiently larger than the FWHM of the beam size of the WIDE-L band ($\sim 58''$; Kawada et al. 2007), thus the presence of the far-infrared emission in between the two nebulae is not spurious. It can be surmised that the region is a dark nebula filled with dust grains. The region around source F in figure 1b also appears dark in the optical image, suggesting that source F is surrounded by a large amount of dust.

The mid-infrared color variation, the location of early-type stars, and the distribution of red objects strongly suggest that YSOs are being born in the region on the north-east side of the arcs. Their formation may be triggered by the existing early-type stars and star-formation is propagating from south-west to north-east. This picture is revealed by the high spatial resolution (especially in $11\ \mu\text{m}$) and the multi-band (especially 140 or $160\ \mu\text{m}$) infrared data of AKARI. Because of the arc-like shape rather than the cometary shape, it is conjectured that the regions where YSOs are concentrated in IC4954/4955 are not pre-existing clouds imploded and/or evaporated by the effect of stellar winds, such as in the Elephant Trunk Nebula (Reach et al. 2004), but are rather triggered by the ‘collect and collapse’ type mechanism with stellar

winds of the heating stars (Elmegreen 1998). Rather uniformly distributed YSOs may also support this interpretation (e.g., Efremov & Elmegreen 1998).

4.2. *Origin of Roslund 4*

To investigate the origin of the IC4954/4955, mid-infrared maps of the surrounding region of about $1^\circ \times 1^\circ$ at 9 and $18\mu\text{m}$ are created from the IRC all-sky survey data. The S9W/L18W color image is shown in figure 6a with the contours of the $100\mu\text{m}$ data of the IRAS Sky Survey Atlas (ISSA, Wheelock et al. 1994). It indicates that there is a cavity of low mid-infrared emission centered around $(\alpha, \delta) = (20^{\text{h}} 03^{\text{m}}, +29^\circ.00)$ and that the IC4954/4955 region is located on an edge of the cavity. image (figure 1).

To examine and confirm the presence of the cavity, HI 21 cm data of the region are obtained from the Canadian Galactic Plane Survey (CGPS)² and examined. Figure 7 shows a plot of the intensity vs. velocity of the HI data. It indicates that the HI gas in this region has a velocity range of $0\text{--}30\text{km s}^{-1}$. This is in good agreement of the velocity range of CO emission associated this region of $6\text{--}19\text{km s}^{-1}$ (Leisawitz et al. 1989). The HI intensity integrated over $0\text{--}30\text{km s}^{-1}$ is shown in figure 6b, which clearly supports the presence of a low density cavity around the center of the map. In figure 6b also plotted by the crosses are YSO candidates. They are selected from the 2MASS catalog based on the same criteria, $H - K > 0.9$ and $J - H > 0.9$, as in figure 4b. In addition a condition of $13.5 < K < 15.0$ is estimated from the K magnitude of the YSO candidates in figure 4b and applied to exclude foreground and background sources. The symbols α , β , and γ indicate the regions where concentration of YSOs is seen. YSO candidates seem to be located on the edge of the cavity. It is most clearly seen in the eastern edge, which includes the IC4954/4955 region as well as the regions α and β , however, only a few YSOs are found at the north and south edges.

The radius of the cavity is estimated as about 10 pc. The cavity is elongated and partly collapsed. Such structures are commonly seen in Galactic bubbles (Churchwell et al. 2006). The cavity of the IC4954/4955 may have been created by supernovae (SNe) or O-type stars. Progenitor candidates have been searched for in the Tycho-2 spectral type catalog (Wright et al. 2003), All-sky compiled catalog (Kharchenko 2001), Mean radial velocities catalog (Barbier-Brossat & Figon 2000), and SNRs catalog (Green et al. 2006). but any progenitors of such a kind are not found. Any SNR like structures are not found either in the soft X-ray maps of ROSAT or in the NVSS 1.4 GHz map (Condon et al. 1998), although there seem to be some point-like condensations in the region. The cavity of the size of $\sim 40\text{pc}$ in IC1396 is made by a single O6.5 star (Patel et al. 1995). Thus the O8en star located at the south-west of the IC4954/4955 (figure 4b) could be the progenitor because the dense region is spread at the north-east of the cavity. However the star may be too young if the age of Roslund 4 is 15 Myr and the star-formation was delayed relative to the trigger event because of the internal motions

² <http://www.ras.ualgary.ca/CGPS>

(Elmegreen 1998). Since SNRs disappear in the time scale of ~ 1 Myr and the age of the cavity must be older than 4 Myr based on the age of the Roslund 4, it is not unexpected that there is no direct sign for the progenitor. The Cepheus bubble (Patel et al. 1998) is also thought to be formed by O-type stars or supernovae, but shows no direct hint of them. The present AKARI observations have revealed another bubble of small scale, which seems to trigger past (4–15 Myr old) star-formation in IC4954/4955. It also indicates the ‘current star-formation’ in the region, which is triggered by stars of the second generation. This trigger seems to be different from the ‘globule-squeezing’ type in the Elephant Trunk Nebula near the Cepheus bubble. The present observations indicate triggered star-formation over the three generations in a different spatial scale in the IC4954/4955.

5. Summary

With the two scientific instruments (IRC and FIS) on board AKARI we obtained 7 band images of IC4954/4955 from 7 to $160\ \mu\text{m}$ with higher spatial resolution and higher sensitivities than previous observations. Based on these observations we obtained the following results.

(1) The mid-infrared images at 9, 11, and $18\ \mu\text{m}$ reveal several distinct structures in the region. Particularly they show three arc-like structures that seem to have been created by stellar winds from the existing B-type stars. The difference between the S9W ($9\ \mu\text{m}$) and S11 ($11\ \mu\text{m}$) images is not significant, indicating that the variation in the spectrum of 6– $13\ \mu\text{m}$ is not large and that the contribution of line emission from ionized gas, such as [NeII] $12.8\ \mu\text{m}$, is relatively small compared to the UIR band emissions at 6.2, 7.7, and $11.2\ \mu\text{m}$.

(2) The S9W ($9\ \mu\text{m}$) to L18W ($18\ \mu\text{m}$) images appear systematically different from each other. The L18W emission is strong near the exciting stars, whereas the S9W emission is dominant in the surrounding region. The S9W filter probes the UIR band emission more effectively than the IRAS $12\ \mu\text{m}$ because its band profile is shifted to shorter wavelengths. We interpret the systematic mid-infrared color variation in terms of the decreasing contribution of thermal dust emission with the distance from the exciting source. The color variation clearly indicates the location of exciting stars, suggesting that the star-formation in IC4954/4955 is progressing from south-west to north-east.

(3) Young stellar objects are distinguishable for the first time at $11\ \mu\text{m}$. They are located in the large S9W to L18W ratio regions, suggesting that current star-formation has been triggered by previous star-formation activities.

(4) The FIS data allow to correctly estimate the total infrared luminosity from the region, which is about one sixth of the energy emitted from the existing early-type stars. Thus there is little possibility that embedded luminous stars have escaped detection. It also suggests that the total dust mass of the infrared emission is about $60\ M_{\odot}$. The 140 and $160\ \mu\text{m}$ images reveal the presence of a high density region between IC4954 and IC4955, which is also supported by optical images.

(5) The IRC all-sky survey data together with the HI 21 cm data further suggest the presence of a bubble-like structure of a degree scale, on whose edge the IC4954/4955 region is located, indicating triggered star formation over three generations.

The IC4954/4955 region is not a massive star-formation region, and is currently populated by B-type stars. The mass of the infrared emitting material is also not huge. The suggested hole of the interstellar matter is not large and thus should be created by a less energetic event compared to IC1396. The present observations suggest that even in such a moderate star-forming region, the sequential star-formation occurs and is on-going at present. Medium-scale star-formation could be common and should be studied in future investigations.

AKARI continues to provide significant data for the study of interstellar medium and star forming regions owing to its high sensitivity, wide wavelength coverage and wide mapping capability, during the course of its mission.

AKARI is a JAXA project with the participation of ESA. We thank all the members of the AKARI project for their continuous help and support. We thank T. Negishi, I. Maeda, H. Mochizuki, K.-W. Chan, S. Fujita, C. Ihara, H. Ikeda, T. Yamamuro, and N. Takeyama for their contributions in the development of the IRC and D. Jennings for providing us with the calibration sources. We also thank K. Imai, M. Ishigaki, H. Matsumoto, N. Matsumoto, T. Tange for supporting daily operation of the IRC. The contribution from the ESAC to the pointing reconstruction is greatly acknowledged. We also thank M. Cohen for helping us in the flux calibration, T. Muller for providing us the fluxes of asteroids at the observing times, G. White for careful reading of the manuscript, and T. L. Roellig for the IRS spectrum of the cirrus cloud. We also thank M. Oyadomari, S. Sugiyama, K. Mizushima, T. Tohma, N. Shigemoto, M. Tomizawa, M. Shinano, M. Suzuki, M. Akutagawa especially for supporting critical phase of AKARI as well as supporting long-term pre-flight tests. We also thank S. Arimura, K. Ito, T. Murakami, for supporting daily operation of the AKARI. We thank H. Iida, K. Higashino, K. Sato, A. Genba, N. Sumi and C. Ihara, and all the members of the altitude and orbit control team, for giving us the advices in the re-construction of the initial data as well as pre-flight and post-flight daily hard works. We also thank S. Yoshida, Yu. Ochi, Yo. Ochi, K. Okamoto, S. Tsunematsu, and all the members of the cryogenic team for supporting long-term pre-flight cooling tests. W.K., I.S., and T.T. have been financially supported by the Japan Society of Promotion of Science (JSPS). This work is supported in part by a Grant-in-Aid for Scientific Research on Priority Areas from the Ministry of Education, Culture, Sports, Science, and Technology of Japan and Grants-in-Aid for Scientific Research from JSPS.

The research presented in this paper used data from the Canadian Galactic Plane Survey, a Canadian project with international partners, supported by the Natural Sciences and Engineering Research Council. We also made use of the ROSAT Data Archive of the Max-Planck-Institut für extraterrestrische Physik (MPE) at Garching, Germany.

References

- Barbier-Brossat, M., Figon, P., 2000, A&AS, 142, 217
- Benjamin, R., A. et al. 2003, PASP, 115, 953
- Boulanger, F. et al. 1988, ApJ, 332, 328
- Churchwell, E., et al. 2006, ApJ, 649, 759
- Clarke, A. J., Oudmaijer R. D. and S. L. Lumsden, 2005, MNRAS, 363, 1111
- Cohen, M., et al. 1999, AJ, 117, 1864
- Cohen, M., Megeath, S. T., Hammersley, P. L., Martin-Luis, F., & Stauffer, J., 2003, AJ, 125, 2645
- Condon, J. J., Cotton, W. D., Greisen, E. W., Yin, Q. F., Perley, R. A., Taylor, G. B., & Broderick, J. J. 1998, AJ, 115, 1693
- Coté, J., & van Kerkwijk, M. H., 1993, A&A, 274, 870
- De Jager, C., & Nieuwenhuijzen, H, 1987, A&A, 177, 217
- Delgado, A. J., Miranda, L. F., Fernandez, M., Alfaro, E. J., 2004, AJ, 128, 330
- Efremov, Y. N., & Elmegreen, B. G. 1998, MNRAS, 299, 643
- Elmegreen, B. G. 1998, in *Origins*, ed. C. E. Woodward, J. M. Shull, & H. A. Thronson, Jr., ASP Conf. ser. 148, 150
- Green, D. A., 2006, *A Catalogue of Galactic Supernova Remnants (2006 April version)* Laboratory, Cambridge, United Kingdom (available at "<http://www.mrao.cam.ac.uk/surveys/snrs/>").
- Habing, H. J. 1968, Bull. Astron. Inst. Netherlands, 19, 421
- Hildebrand, R. H. 1983, QJRAS, 24, 267
- Ishihara, D., et al. 2003, Proc. of SPIE, 4850, 1008
- Ishihara, D., et al. 2006a, PASP, 118, 324
- Ishihara, D., et al. 2006b, AJ, 131, 1074
- Ishihara, D., et al. 2007, in prep.
- Johnson, H. L., 1966, ARA&A, 4, 193
- Kaneda, H., et al. 2007b, PASJ, this volume, #3067
- Kawada, M., et al. 2007, PASJ, submitted
- Kharchenko, N. V., 2001, *Kinematika i Fizika Nebesnykh Tel*, 17, 5, 409
- Kerton, C. R., 2002, AJ, 124, 3449
- Leisawitz, D., & Hauser, M. G. 1988, ApJ, 332, 954
- Leisawitz, D., Bash, F. N., and Thaddeus P., 1989, ApJS, 1989, 70, 731
- Makiuti, S., 2007, PASJ, submitted
- Merrill, P., W., Burwell, C., G., & Miller, W., C., 1942, ApJ, 96, 15
- Mizutani, M., Onaka, T., & Shibai, H. 2004, A&A, 324, 579
- Murakami, H., et al. 2007, PASJ, submitted
- Nakagawa, T., et al. 2007, PASJ, submitted
- Neugebauer, G., et al. 1984, ApJL, 278, L1
- Onaka, T. 2004, in *Astrophysics of Dust*, ASP Conf. ser. 309, 163
- Onaka, T., Tokura, D., Sakon, I., Tajiri, Y. Y., Takagi, T. & Shibai, H. 2007a, ApJ, 654, 844
- Onaka, T., et al. 2007b, PASJ, this volume
- Oudmaijer, R. D. & Dolf de Winter, 1995, A&A, 295, L43

- Patel, N. A., Goldsmith P. F., Heyer M. H., Snell R. L., & Pratap P., 1998, ApJ, 507, 241
- Patel, N. A., Goldsmith P. F., Snell R. L., Hezel T., & Xie T., 1995, ApJ, 447, 721
- Phelps R. L., 2003, AJ, 126, 826
- Price, S. D., et al. 2001, AJ, 121, 2819
- Racine, R. 1969, AJ, 74, 816
- Reach, W. T., et al. 2004, ApJS, 154, 385
- Rieke, G. H., & Lebofsky, M. J. 1985, ApJ, 288, 618
- Roslund, C. 1960, PASP, 72, 205
- Ryter, C., Puget, J. L., Mérault, M., 1987, A&A, 186, 312
- Sakon, I., et al. 2006, ApJ, 651, 174
- Schmidt-Kaler, Th. 1982, *Landolt-Börnstein: Numerical Data and Functional Relationships in Science and Technology*, edited by K. Schaifers and H.H. Voigt (Springer-Verlag, Berlin), VI/2b
- Suzuki, J., 2007, PASJ, submitted
- Taylor, A. R., Goss, W. M., Coleman, P. H., van Leeuwen, J., & Wallace, B. J., 2003, AJ, 125, 3145
- Taylor, A. R., 2003, AJ, 125, 3145
- Tielens, A. G. G. M., & Hollenbach, D. 1985, ApJ, 291, 747
- Wheelock, S. L., et al. 1994, *IRAS Sky Atlas Explanatory Supplement* (Publ. 94-11, Pasadena: JPL)
- Whitney, B. A., Wood, K., Bjorkman, J. E., & Cohen, M., 2003, ApJ, 598, 1079
- Wright, C. O., Egan, M. P., Kraemer, K. E., & Price, S. D., 2003, AJ, 125, 359

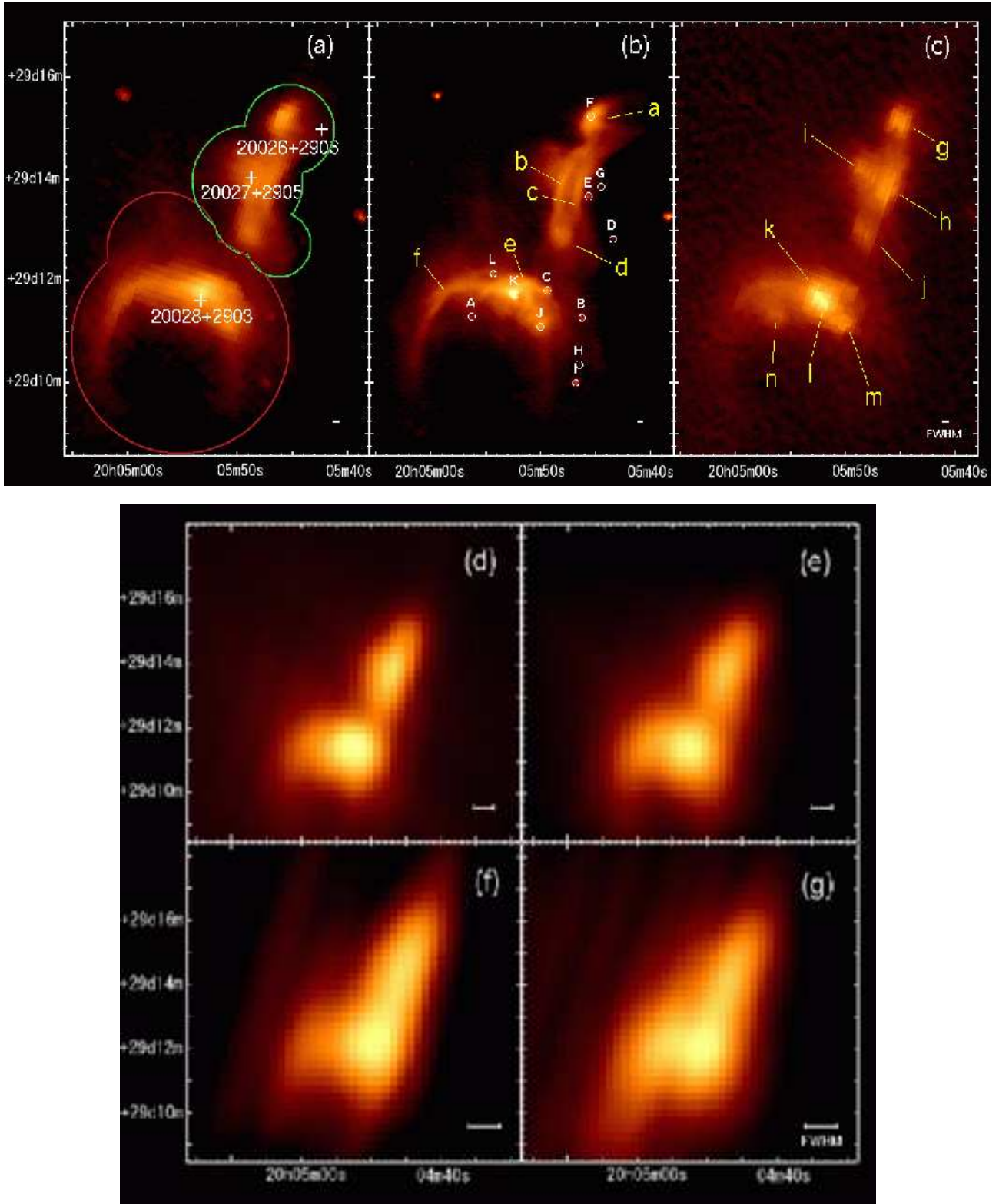


Fig. 1. IC4954/4955 images by AKARI observations: (a) S9W ($9\mu\text{m}$), (b) S11 ($11\mu\text{m}$), (c) L18W ($18\mu\text{m}$), (d) N60 ($65\mu\text{m}$), (e) WIDE-S ($90\mu\text{m}$), (f) WIDE-L ($140\mu\text{m}$), and (g) N160 ($160\mu\text{m}$) bands in the equatorial (J2000) coordinates. The integrated areas in the photometry for each nebula are shown on the S9W image (a) with the red line for IC4954 and the green line for IC4955. Three IRAS point sources are also indicated by the plusses. The symbols $a-f$ in the S11 (b) and $g-n$ in the L18W (c) indicate distinct structures in the images. The symbols A–L show point-like sources in the S11 image (b).

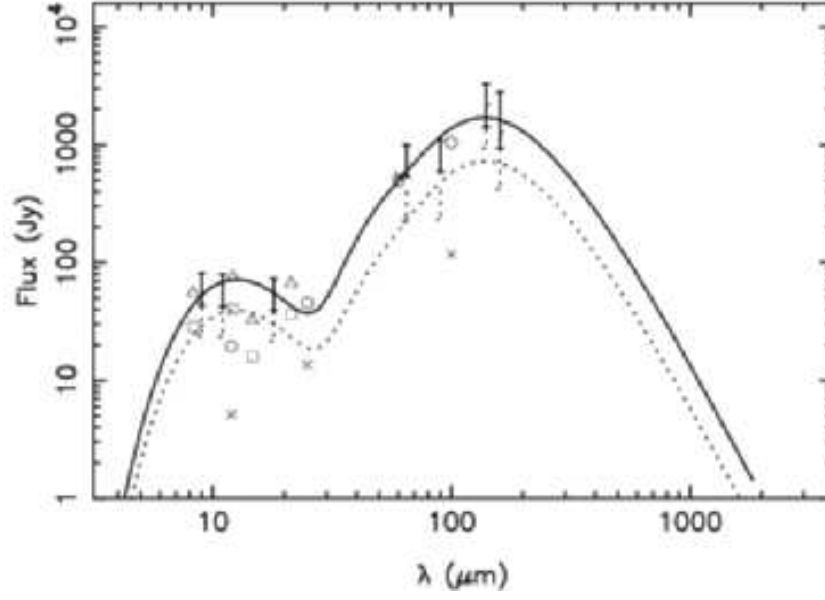


Fig. 2. The 9–160 μm spectral energy distribution of IC4954 and IC4955 measured by AKARI. The solid bars show the observational data for IC4954 and the dotted bars for IC4955 derived from the AKARI observations. The triangles and squares indicate those estimated from the MSX data for IC4954 and IC4955, respectively. The circles and crosses are those from the IRAS PSC data for IC4954 and IC4955, respectively (see text for details). The solid and dotted curves are fitted 3-temperature dust models (see also text).

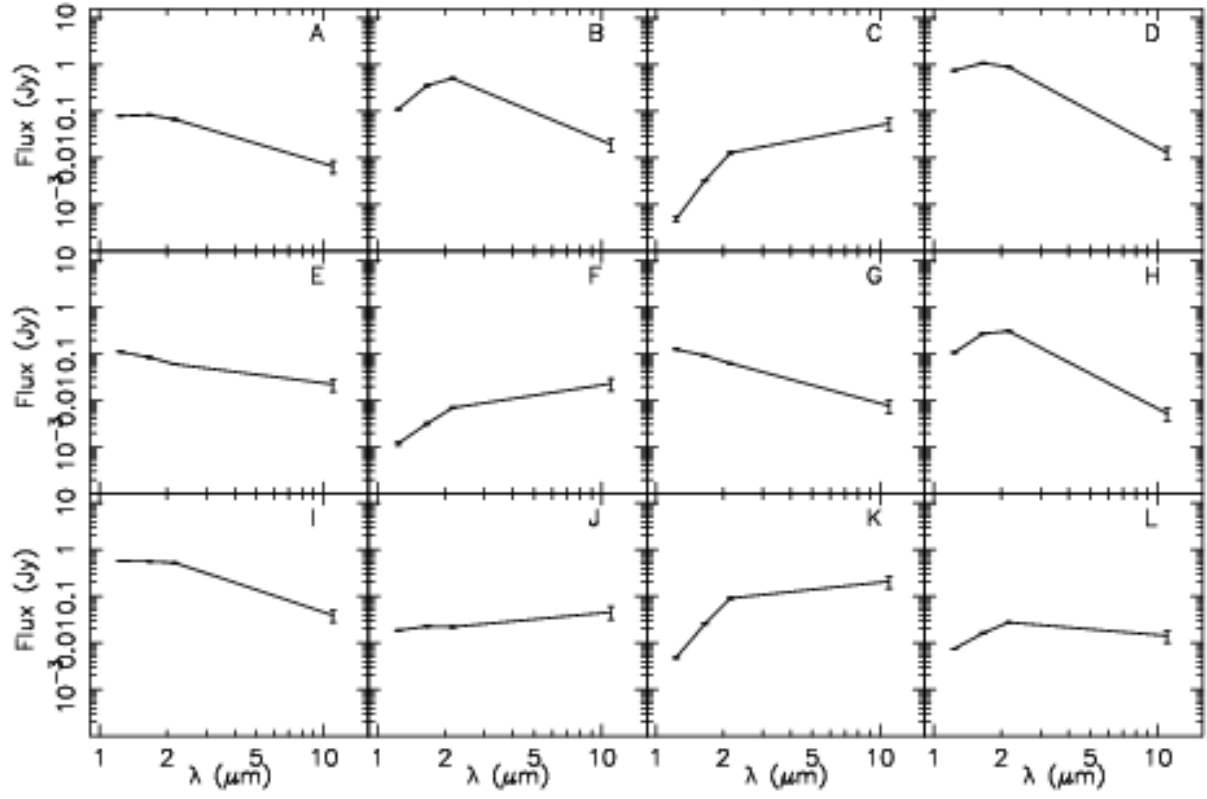


Fig. 3. Spectral energy distribution in the near- to mid-infrared of 12 detected sources in the S11 image (figure 1). The J, H, and K data are taken from the 2MASS catalog.

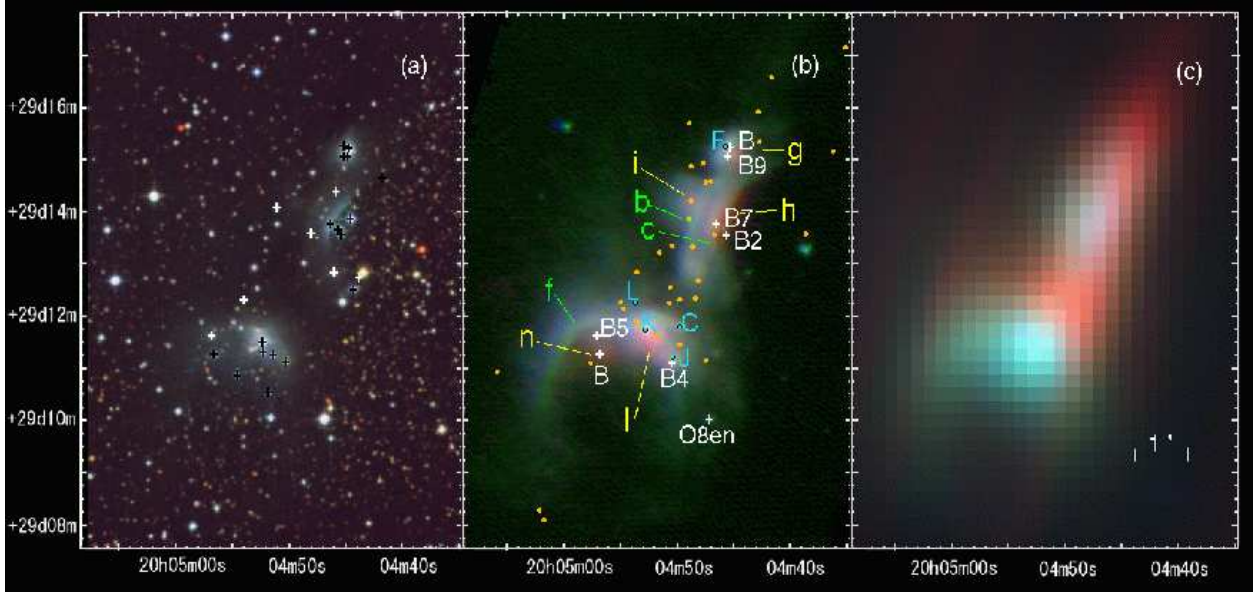


Fig. 4. Synthesized color images of IC4954/4955 in the equatorial coordinates: (Left) Optical three-color image of B (blue), R (green) and Z (red) of the DSS image; (Middle) mid-infrared three-color image made from the S9W (blue), S11 (green) and L18W (red) images taken with the AKARI/IRC. Optically known early-type stars are indicated by the crosses with the spectral types (Delgado et al. 2004; Merrill et al. 1942). The symbols of C, F, J, K, and L in blue show point-like objects in the S11 image, $a-f$ (green) indicate structures seen in the S9W or S11 images, and $g-n$ (yellow) denote structures seen in the L18W image as depicted in figures 1b and c. Red ($H - K > 0.9$ and $J - H > 0.9$) sources selected from the 2MASS catalog are shown by the orange circles. The spectral types of the stars are indicated in white. (Right) Far-infrared three-color image of IC4954/4955 made from the N60 (blue), WIDE-S ($90\,\mu\text{m}$) (green) and WIDE-L ($140\,\mu\text{m}$) (red) images taken with the AKARI/FIS.

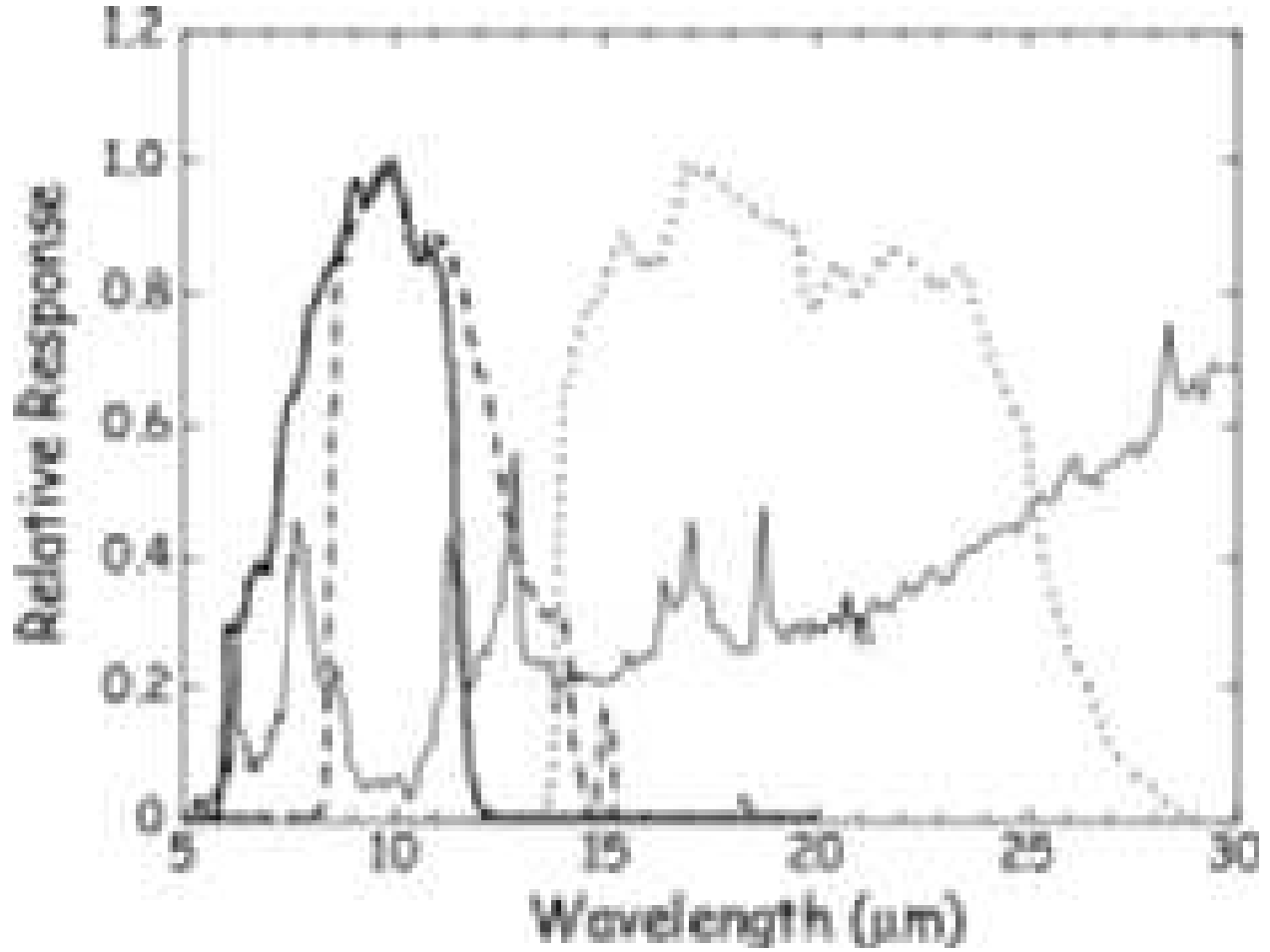


Fig. 5. Relative band response of the S9W (thick solid line), S11 (thick dashed line), and L18W (thick dotted line) in units of electron/energy normalized at the peak. An interstellar cirrus spectrum at $(l, b) = (355.^{\circ}2, 0.^{\circ}02)$ taken with *Spitzer/IRS* is also shown as a reference by the thin solid line. It is in units of Jy, but arbitrarily scaled.

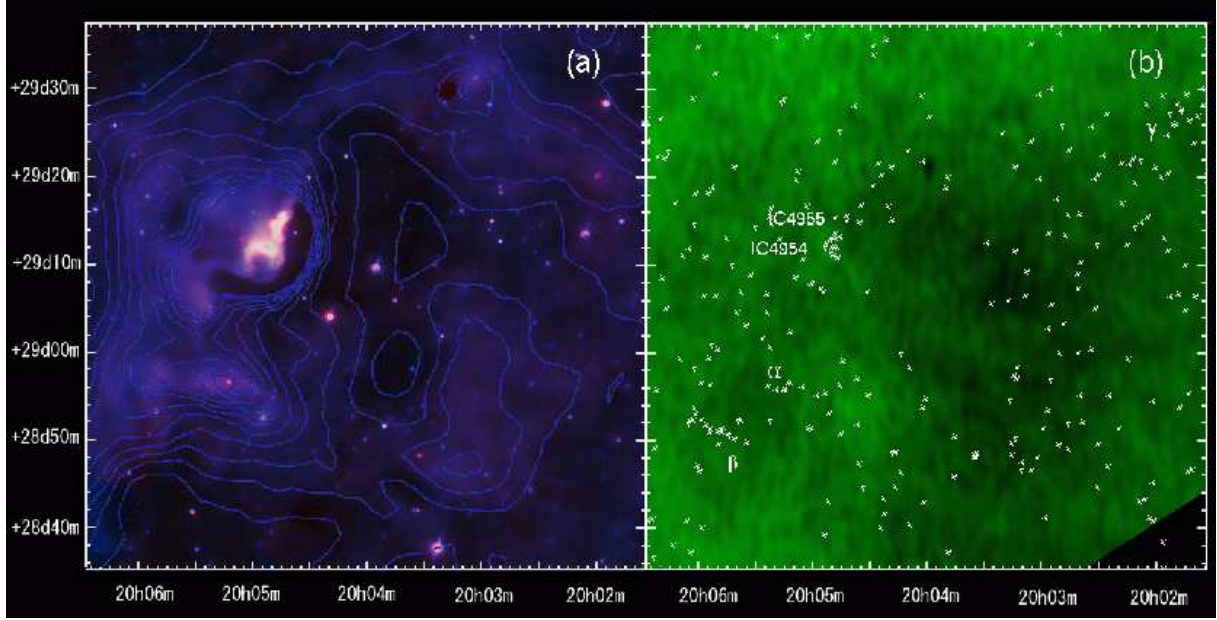


Fig. 6. (Left) Color image made from the S9W and L18W all-sky survey data of AKARI/IRC around IC4954/4955. The contours indicate the ISSA $100\mu\text{m}$ intensity. (Right) CGPS HI 21cm map integrated over the velocity range of $0\text{--}30\text{ km s}^{-1}$ (see text). The crosses indicate red sources selected from the 2MASS catalog.

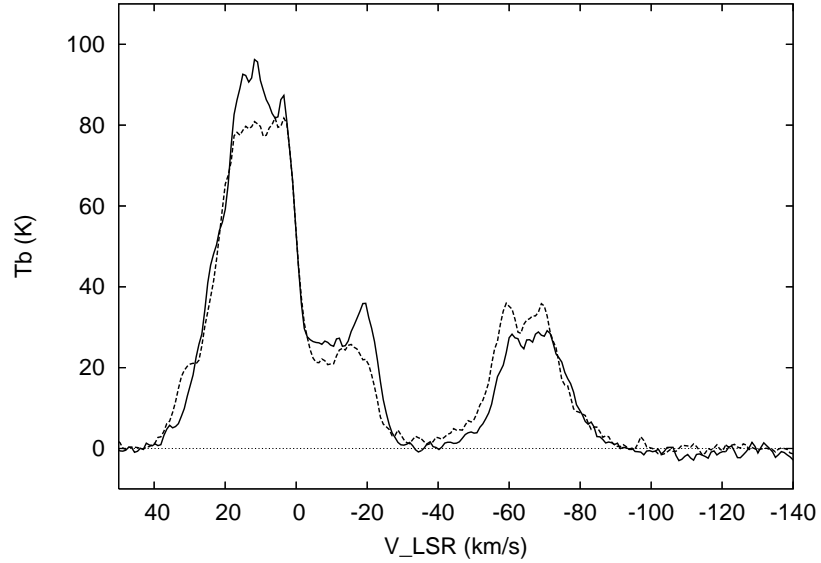


Fig. 7. Intensity vs velocity plot of the HI 21cm data (CGPS). The solid line indicates at the IC4954/4955 region, whereas the dashed line corresponds to the center of the cavity (figure 6).